Faraday Discussions

Accepted Manuscript

CREATED USING THE RSC LaTeX PCCP ARTICLE TEMPLATE – SEE www.rsc.org/electronicfiles FOR DETAILS

PAPER www. rsc.org/faraday_d | Faraday Discussions

Ultrafast dynamics of nanoplasmonic stopped-light lasing

Sebastian Wuestner,[a] Tim Pickering,[a] Joachim M. Hamm,[a] A. Freddie Page,[a] Andreas Pusch[a] and Ortwin Hess*[a]

Received Xth XXXXXXXXXX 20XX, Accepted Xth XXXXXXXXX 20XX

First published on the web Xth XXXXXXXXXX 20XX

DOI: 10.1039/c000000x

We study the spatio-temporal dynamics of coherent amplification and lasing in planar gain-enhanced nanoplasmonic structures and show that a singularity in the density of optical states leads to a stopped-light feedback mechanism that allows for cavity-free photonic and surface-plasmon polariton nanolasing. We reveal that in the absence of cavity-induced feedback a phase-locked superposition of quasi dispersion-free waveguide mode promotes the dynamic formation of a subwavelength lasing mode. Simulations on the basis of a full-time domain Maxwell-Bloch Langevin approach uncover a high spontaneous emission factor $\beta \approx 0.9$ and demonstrate that the stopped-light lasing/spasing mechanism is remarkably robust against interface roughness. Stopped-light surface-plasmon polariton lasing is shown to be stable for gain sections of a width of down to 200 nm but in wider gain structures of the order of 1 μm the dynamics is characterised by spatio-temporally oscillating lasing surface-plasmon polaritons with typical temporal and spatial periods of smaller than 5 fs and smaller than 100 nm. Stopped-light lasing thus provides opportunities for ultrafast nanolasing and the realization of ultra-thin lasing surfaces and offers a new route to ultrafast spasing and cavity-free active quantum plasmonics.

1 Introduction

Lasers have had tremendous impact on research and technology and have become an essential component of everyday life. Through innovative design concepts, new materials as well as advancements in fabrication techniques they have become ever more powerful, enter new frequency domains and emit shorter and shorter pulses. At the same time, it was also possible to allow lasers to become smaller and smaller to recently culminate in an experimental demonstration of subwavelength nanolasing[1–6]. This miniaturisation was achieved through significant innovation in the two key ingredients that constitute lasers: light amplification and feedback. Semiconductor gain materials such as quantum wells and dots proved as important in this shrinking process as did innovative microcavity resonator designs[7], for example, in the form of microdisks[8], micropillars[9], defect

[a] *The Blackett Laboratory, Department of Physics, Imperial College London, South Kensington Campus, London SW7 2AZ, United Kingdom. Fax: +44 20 7594 2077; Tel: +44 20 7594 7586; E-mail: o.hess@imperial.ac.uk*

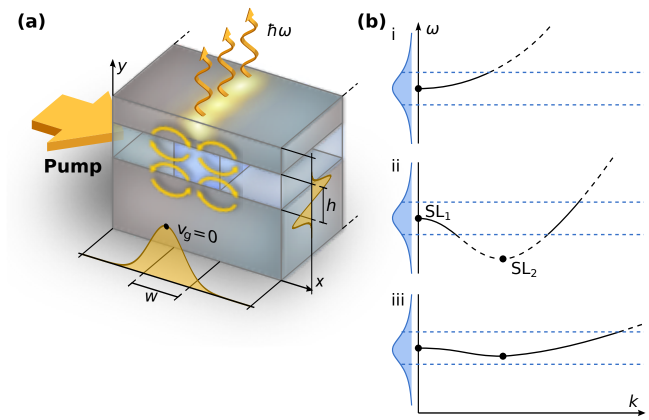

Fig. 1 (a) Subwavelength localised vortex-lasing in a stopped-light design based on a gain-enhanced plasmonic heterostructure. The stopped-light feature of the design allows for the trapping of photons in a closed vortex visualised by paired semi-circular yellow arrows. Exploiting leaky-modes, emission into free space takes place perpendicular to the surface. (b) By engineering the band structure of the metal-dielectric waveguide, several stopped-light points can be made to fall within the gain spectrum, resulting in a flat dispersion with an average slope of $(\omega_2-\omega_1)/(k_2-k_1)$.

mode photonic crystals [10,11] and photonic nanowires.

Recent plasmonic nanolasers employ plasmonic resonances for feedback [12–15], allowing them to concentrate light into mode volumes that are no longer limited by diffraction. The use of localised surface plasmon resonances as cold-cavity modes, however, is only one route to lasing on subwavelength scales. Indeed, Lasing does not require modes predefined by a resonator with a particular geometry but only a feedback mechanism (which traditionally is a resonator). However, let us consider the situation in a random laser. There, feedback arises from multiple random scattering events that lead to the spontaneous formation of closed optical paths within the disordered medium [16,17]. Recently, we have shown that cavity-free lasing is not restricted to micrometer sizes in disordered media (using random feedback) but can also be realised on subwavelength (nano-) scales using stopped light to provide *local feedback* [18]. Having established this principle and identified its main physical properties, we here study the spatio-temporal dynamics of a stopped-light (SL) laser as illustrated in Fig. 1 and uncover the ultrafast spatio-temporal dynamics of SL surface-plasmon polariton (SPP) lasing with <5 femtosecond dynamics on scales of less than 100 nm in a structure designed to support SPP modes.

2 Maxwell-Bloch Langevin theory

In the following we will briefly outline the Maxwell-Bloch Langevin approach which forms the bias for the time-resolved simulations discussed here. This involves, in particular, combining the Finite-Difference Time-Domain (FDTD) method with auxiliary differential equations that self-consistently describe both, the material dispersion of the plasmonic cladding and the nonlinear, spatially resolved polarization response of the gain media.

In framework of the Maxwell-Bloch formalism we model the gain medium as a four-level system with pump ($0 \rightarrow 3$) and emission ($2 \rightarrow 1$) transitions [19]. These optical transitions are connected by and with (coherent) polarization densities $\mathbf{P}_a(\mathbf{r},t)$ and $\mathbf{P}_e(\mathbf{r},t)$ whose dynamics can be described on the basis of the differential equations

$$\begin{aligned} \frac{\partial^2 \mathbf{P}_{\mathrm{a,e}}}{\partial t^2} + 2\gamma_{\mathrm{a,e}} \frac{\partial \mathbf{P}_{\mathrm{a,e}}}{\partial t} + \omega^2_{\mathrm{a,e}} \mathbf{P}_{\mathrm{a,e}} &= -\sigma_{\mathrm{a,e}} \Delta N_{\mathrm{a,e}} \mathbf{E} \\ &- \kappa_{\mathrm{a,e}} \left[\omega_{\mathrm{a,e}} \mathrm{Im}\left(\mathbf{F}_{\mathrm{a,e}}\right) + \frac{\partial \mathrm{Re}\left(\mathbf{F}_{\mathrm{a,e}}\right)}{\partial t} \right] . \quad (1) \end{aligned}$$

These equations model the dynamics of spatio-temporal light-matter interaction via dipole coupling of the electric field to the electronic transitions. The resonance frequencies ω_i (and transition frequencies $\omega_{r,i} = \sqrt{\omega^2 - \gamma_i^2}$), the spectral half-widths γ_i, the phenomenological coupling constants $\sigma_i = 2\varepsilon_0 n_s' c \gamma_i \sigma_{0,i}$ (that are associated with the emission and absorption cross-sections $\sigma_{0,i}$), as well as the real part of the host refractive index n_s' reflect the particular choice of gain material.

The spatio-temporal dynamics of the occupation densities N_0 to N_3, which, in turn, determine the inversions $\Delta N_{\mathrm{e}}(\mathbf{r},t) = N_2(\mathbf{r},t) - N_1(\mathbf{r},t)$ and $\Delta N_{\mathrm{a}}(\mathbf{r},t) = N_3(\mathbf{r},t) - N_0(\mathbf{r},t)$ for emission and absorption, is given by the set of equations

$$\frac{\partial N_3}{\partial t} = \frac{1}{\hbar\omega_{\mathrm{r,a}}} \left(\frac{\partial}{\partial t} \mathbf{P}_{\mathrm{a}} + \gamma_{\mathrm{a}} \mathbf{P}_{\mathrm{a}} \right) \cdot \mathbf{E} - \frac{N_3}{\tau_{30}} - \frac{N_3}{\tau_{32}} + F_{33} \,, \quad (2)$$

$$\frac{\partial N_2}{\partial t} = \frac{N_3}{\tau_{32}} + \frac{1}{\hbar\omega_{\mathrm{r,e}}} \left(\frac{\partial}{\partial t} \mathbf{P}_{\mathrm{e}} + \gamma_{\mathrm{e}} \mathbf{P}_{\mathrm{e}} \right) \cdot \mathbf{E} - \frac{N_2}{\tau_{21}} + F_{22} \,, \quad (3)$$

$$\frac{\partial N_1}{\partial t} = \frac{N_2}{\tau_{21}} - \frac{1}{\hbar\omega_{\mathrm{r,e}}} \left(\frac{\partial}{\partial t} \mathbf{P}_{\mathrm{e}} + \gamma_{\mathrm{e}} \mathbf{P}_{\mathrm{e}} \right) \cdot \mathbf{E} - \frac{N_1}{\tau_{10}} + F_{11} \,, \quad (4)$$

$$\frac{\partial N_0}{\partial t} = \frac{N_1}{\tau_{10}} + \frac{N_3}{\tau_{30}} - \frac{1}{\hbar\omega_{\mathrm{r,a}}} \left(\frac{\partial}{\partial t} \mathbf{P}_{\mathrm{a}} + \gamma_{\mathrm{a}} \mathbf{P}_{\mathrm{a}} \right) \cdot \mathbf{E} + F_{00} \,. \quad (5)$$

The lifetimes τ_{jk} account for non-radiative relaxation processes between the levels. The term linked with the polarization density of the absorption transition, $(\hbar\omega_{\mathrm{r,a}})^{-1}(\partial \mathbf{P}_{\mathrm{a}}/\partial t + \Gamma_{\mathrm{a}} \mathbf{P}_{\mathrm{a}})\mathbf{E}$ represents the spatially and temporally inhomogeneous excitation. Quantum fluctuations and amplified spontaneous emission are represented via Langevin noise terms given by $\mathbf{F}_{\mathrm{e}}(\mathbf{r},t)$, $\mathbf{F}_{\mathrm{a}}(\mathbf{r},t)$, and $F_{00}(\mathbf{r},t)$ to $F_{33}(\mathbf{r},t)$ [18,19]. Below lasing threshold the noise acts as source for amplified spontaneous emission giving rise to the recorded background spectra, while above the lasing threshold, the noise acts as a seed aiding the transient build-up of the coherent lasing fields through feedback and stimulated emission processes in the gain medium.

3 Dispersionless stopped light in metal-dielectric waveguides

In our study of the characteristic spatio-temporal dynamics of stopped-light nanolasing we adopt, for specificity, the geometry as introduced in [18] and illustrated in

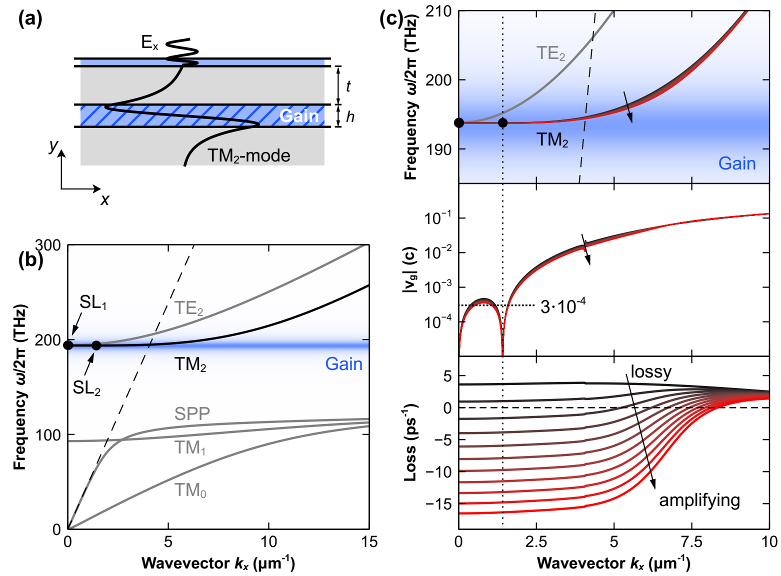

Fig. 2 (a) Field profile of the TM_2 mode at 1547 nm in a plasmonic heterostructure with $h = 290$ nm and $t = 500$ nm. (b) (Complex-frequency) dispersion of the structure, highlighting the wavevector dependence of the weakly-leaky TM_2 mode that includes two SL points in red. The gain spectrum is highlighted in blue. (c) Impact of small-signal gain on the dispersion, group velocity and loss of the TM_2 mode from no gain (black) to a gain coefficient of 4180 cm^{-1} (red).

Symbol	Description	Value
$\omega_e/2\pi$ (λ_e)	Emission frequency (wavelength)	193.41 THz (1550 nm)
γ_e	Emission spectral half-width	$1/(40\,\text{fs}) = 25\,\text{ps}^{-1}$ ($\sim$32 nm)
$\sigma_{0,e}$	Emission cross-section	$2.09\cdot10^{-15}\,\text{cm}^2$
N	Carrier density	$2\cdot10^{18}\,\text{cm}^{-3}$
g_e	Maximum gain coefficient	$4180\,\text{cm}^{-1}$

Table 1 Gain medium parameters for emission into the leaky TM_2 waveguide mode.

Fig. 2. It consists of a planar metal-dielectric-metal stack with a top metal layer of thickness $t = 500$ nm and a waveguide core of height $h = 290$ nm on top of a thick metal substrate (Fig. 2a). The dielectric permittivities of the core and cladding materials are chosen to be characteristic of III-V semiconductors (such as InGaAsP) and transparent conductive oxides (indium tin oxide), respectively, giving rise to a (weakly) leaky TM_2 mode in the dispersion diagram (Fig. 2b).

By design this dispersion has two stopped-light singularities that lie close in frequency: SL_1 at $\omega_1/2\pi = 193.8$ THz ($\lambda_1 = 1546.9$ nm) and $k_1 = 0$ and SL_2 at $\omega_2/2\pi = 193.78$ THz ($\lambda_2 = 1547.06$ nm) and $k_2 = 1.42\,\mu m^{-1}$. With both SL singularities being to the left of the (dashed) light-line, the SL lasing mode will couple to free-space radiation (perpendicular to the plane). The emission of light amounts to around 3-4% of the total energy lost per cycle and can be controlled by adjusting the thickness of the top metal cladding. We will start our discus-

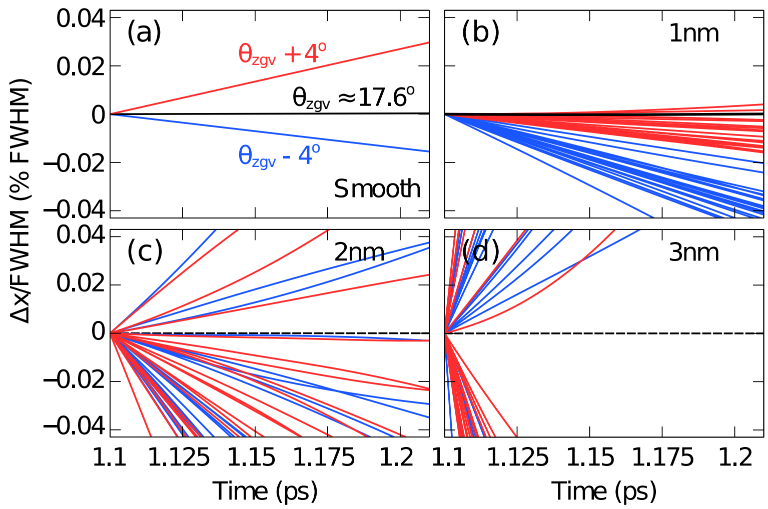

Fig. 3 Change in the centre of energy position of wavepackets excited in the heterostructure waveguides with smooth (a) and rough interfaces (1−3 nm rms height, b-d). Red lines indicate wavepackets incoupled at an angle of incidence $\theta = \theta_{ZGV} + 4\,\text{deg}$, while blue lines correspond to an incidence angle $\theta = \theta_{ZGV} - 4\,\text{deg}$. For cases (a,b) an optimal angle has been found corresponding to near zero propagation shown by the solid black lines. The dashed black lines in (c,d) mark the zero position.

sion by initially highlighting the characteristics of this photonic (i.e., leaky) design, before we will concentrate our discussion on analysing the spatio-temporal lasing/spasing dynamics of stopped surface-plasmon polaritons (i.e., spasing[12]) where multiple SL singularities fall onto a bound plasmonic mode.

Fig. 2b) shows that based on a passive mode theory we are to expect an extended band of vanishing dispersion. A small-signal gain analysis, where we assume that the gain medium fills the dielectric core of the structure except for a 10nm buffer next to the metal (to account for gain quenching in close vicinity to the metal) confirms that the two SL singularities effectively pin down the dispersion between them and no significant change of the modal dispersion is observed with increasing inversion (Fig. 2c). The modal loss, on the other hand, displays a significant dependence on the inversion and changes sign at $\Delta N_{\text{th}} \approx 0.13$ (Fig. 2c, bottom). This is the point at which the mode is undamped and experiences an almost uniform level of gain over a broad range of k-values (up to $k \approx 5\,\mu\text{m}^{-1}$. As the loss rate includes both dissipative and radiative (leakage through the cladding layer) contributions, we can associate ΔN_{th} with the threshold inversion required for lasing.

So far, we have assumed that all interfaces and surfaces are ideally flat. However, it has been shown that even small structural imperfections can potentially have a significant (detrimental) impact on the propagation characteristics, particularly for light near SL points in slow light devices[20]. This is particularly challenging in photonic crystal waveguides where the disorder-increased light-scattering at interfaces not only imposes limitations on the achievable group index but can also result in Anderson localization of light[21]. In metal dielectric

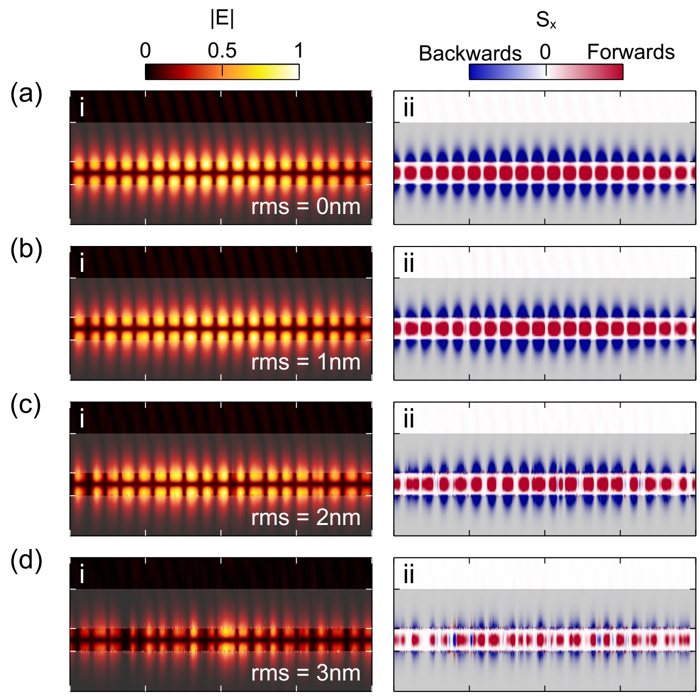

Fig. 4 Electric field amplitude (a.i-d.i) and the x-component of the Poynting vector (a.ii-d.ii) in the heterostructure waveguide with smooth interfaces (a) and rough interfaces with rms = 1 nm (b), 2 nm (c) and 2 nm (d). Higher electric field amplitudes are shown in lighter colours. Grey boxes highlight the positions of the ITO layers.

heterostructures as considered here, however, stopped light arises from a very different effect – negative energy flow inside the metallic cladding[22] and not from backscattering at geometric features as it is the case e.g. in photonic crystals[20]. This remarkable resilience of SL points to surface roughness has recently been observed in a passive metal-dielectric heterostructure[22].

Fig. 3) illustrates the change of the centre of energy position of stopped-light wave packets without gain material where we inject wave packets at two distinct angles corresponding to wavevectors either side of the second SL point. We find that, below a critical rms roughness value, the energy velocity remains constant in time with a clear dependence on the injection angle and one can always find an optimum excitation angle for which the energy velocity along the waveguide direction is zero. It is apparent from the figure that the optimal angle depends on the level of surface roughness and additionally varies from sample to sample. This work up to an rms surface roughness of bout 3 nm where the nature of pulse propagation is changed dramatically: the energy velocity is not constant any more and the pulse is equally likely to propagate in a forwards or backwards direction. In this regime, the propagation of energy is diffusive and correlates only weakly with the waveguide dispersion. As a result of the strong scattering at the surface inhomogeneities one observes a pulse breakup and the disappearance of the global SL point.In the active case with a gain material incorporated into the waveguides we found that SL lasing remains resilient to surface roughness with almost no variation in the average loss rate below rms values less than 1.5 nm [18]. However, above this rms value both the average loss rate and standard deviation steadily rose. The higher losses were seen to arise primarily from the scattering of the modal fields at the rough interfaces and an increased absorption of energy at hotspots, surface irregularities over which the SL mode localises as observed in the mode profiles for different levels of rms roughness (Fig. 4).

4 Spatio-temporal dynamics of stopped-light lasing

Having established the foundations for stopped-light lasing by passive and small signal gain analysis we now perform first-principles time-domain simulations taking into account the full spatio-temporal nonlinearity of the gain material as well as the spatio-temporal interplay between light-field and inversion (Fig. 5). We model the gain material through four-level Maxwell-Bloch-Langevin equations [14,18] (section 2) with parameters that match those used in the semi-analytical mode calculations above. Initially the gain section shall be confined to a 400 nm wide strip, approximately four times smaller than the vacuum wavelength at the SL points. By design the gain section can be pumped optically using a propagating waveguide mode at a higher frequency. Subsequently we will establish a link between newly derived stopped-light laser rate equations to well-established rate-equation approaches for traditional lasers. The difference between the two will then reveals the particular feature of stopped-light nanolasing and a comparison between the spatially resolved Maxwell-Bloch simulations and the stopped-light lasing rate equation model allows us, in turn, to extract effective parameters of the system. We are particularly interested in the confinement factor and the effective mode volume of SL lasing.

4.1 High-β lasing through locking of spatial modes

At a pump level well above threshold, the transient field and inversion dynamics of a typical stopped-light laser can display ultrafast relaxation oscillations with a period of only around 10 ps [18], gradually settling down to a quasi-steady-state. The SL-laser output energy follows a familiar S-shaped input-output curve (Fig. 5a) with a threshold pump rate $r_\mathrm{p} \approx 1.43\,\mathrm{ps}^{-1}$. Spectral narrowing of the emission line (compare Fig. 5b and 5c) above the lasing threshold (5c) is due to the build-up of phase coherence in the SL mode, while below threshold (5b)we observe amplified spontaneous emission (ASE) with a spectrum that matches the spectral density of states of the TM_2 mode at $k = 0$.

Owing to a vanishing group velocity of the lasing TM_2 mode, the local density of optical states (LDOS) is strongly enhanced around the frequency of the SL singularities (Fig. 6). The TE_2 mode, which shares the SL singularity at $k = 0$ with the TM_2 mode (Fig. 2), offers a competing channel for spontaneous emission but its LDOS reaches only about 1/10th of the value of the TM_2 mode due to its stronger dispersion. Consequently, 90% of the spontaneous emission are channeled into the dispersionless TM-polarised lasing mode, which is con-

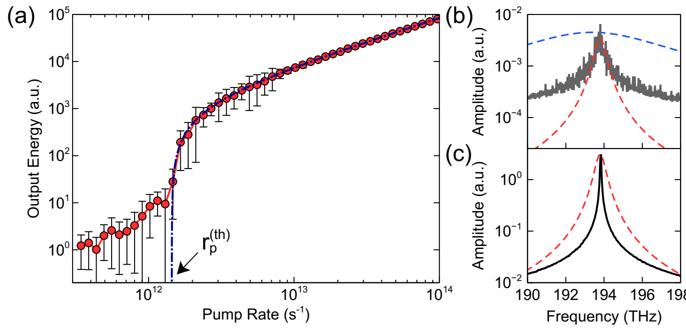

Fig. 5 (a) S-shaped input-output curve of the stopped-light laser with a threshold pump rate $r_p^{(th)} = 1.43\,\mathrm{ps}^{-1}$. The ASE spectrum below threshold (b) can be compared to the lasing spectrum (c), indicating strong spectral narrowing. The spectral width of ASE compares well with the (scaled) spectral density of states of the TM_2 mode at $k=0$ in red, while the gain spectrum in blue is much wider.

firmed by the spontaneous emission factor obtained from the threshold curve, $\beta = \gamma_c/(\gamma_c + \Gamma r_p) \approx 0.9$[23] (total loss rate $\gamma_c \approx 3.71\,\mathrm{ps}^{-1}$). In contrast to micro-cavity lasers, where spontaneous emission channels can be suppressed via cavity design, the concentration of the spontaneous emission into the localised SL lasing mode is a result of the large density of k-modes that fall within the bandwidth of the gain. The observed high-β characteristics and picosecond relaxation oscillations of cavity-free SL lasing can potentially allow for the design of thresholdless plasmonic laser diodes that can be modulated with THz speeds.

4.2 Link to traditional laser models

Laser rate equations are a set of two coupled differential equations that approximate the dynamics of the photon and carrier number[24]. Applied to nanolasers[2,5] this simple model can reproduce the basic characteristics of a laser, such as its threshold behaviour, transient dynamics, and modulation speeds.

Here we start by first noting that Poynting's theorem, which describes the evolution of the electromagnetic energy density $U(\mathbf{r},t)$, can be transformed into a rate equation

$$\frac{\partial S}{\partial t} = -\gamma_c S + R_{\mathrm{stim}}(N)S \qquad (6)$$

for the photon number S at the lasing frequency ω_0 by volume integration of the total energy density,

$$S = (\hbar\omega_0)^{-1}\int_V d^3r\, U(\mathbf{r},t). \qquad (7)$$

This equation also defines the cavity loss rate γ_c and the stimulated emission rate $R_{\mathrm{stim}}(N)$. Fast phase-oscillations of the fields $\mathbf{E}$ and $\mathbf{H}$ at the lasing frequency are eliminated through a time averaging over one period and the integration volume V is taken to encompass the full SL lasing structure making the photon number a slowly-varying, effective variable of the system. In dispersive media, the energy

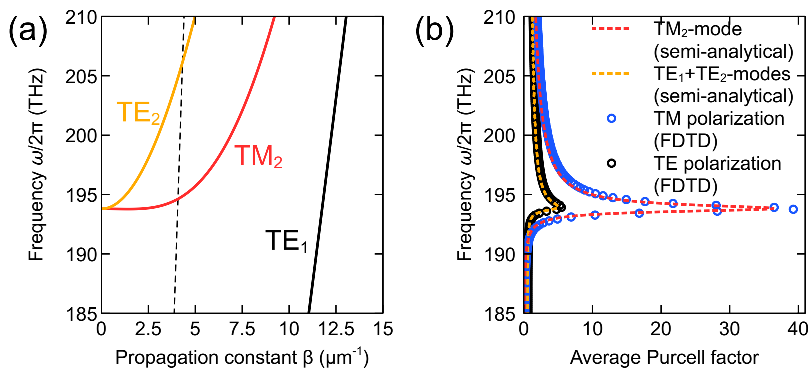

Fig. 6 (a) Dispersion of the TE_1 (orange), TE_2 (black) and TM_2 (red) waveguide modes and (b) the resulting Purcell factor for spontaneous emission into these modes spatially averaged over the position of emitters in the waveguide core. Two separate methods have been used to evaluate the Purcell factor: FDTD simulations (shown by black and blue circles) and semi-analytic calculations based on the waveguide mode dispersion (red and orange dashed lines).

density is given by

$$U(\mathbf{r},t) = U_E(\mathbf{r},t) + U_M(\mathbf{r},t) = \frac{1}{2}\varepsilon_0 \left.\frac{\partial\omega\varepsilon'(\mathbf{r},\omega)}{\partial\omega}\right|_{\omega=\omega_0} \overline{\mathbf{E}^2(\mathbf{r},t)} + \frac{1}{2}\mu_0\overline{\mathbf{H}^2(\mathbf{r},t)} \,. \tag{8}$$

Here, $\varepsilon(\mathbf{r},\omega)$ is the spatially-resolved relative permittivity which follows a Drude dispersion in the metal layers and is equal to ε_a in the active (gain) waveguide core layer (the prime denotes the real part of the complex quantity). It is important to account for the dispersive character of the permittivity to correctly describe the electric energy density U_E, in particular inside metals. In time-domain, this dispersive character is expressed by the dynamic polarization response $\mathbf{P}_f(\mathbf{r},t)$ of the free electron plasma in the metal and its in-phase $\overline{\dot{\mathbf{P}}_f \cdot \mathbf{E}}$ contribution to the electric energy (see Box 1 in Hess et al.[14]).

In Eq. (6), the cavity loss rate γ_c includes both outcoupling of energy from the laser and dissipation of energy inside the laser. The former is connected to the closed contour integral over the Poynting flux, while the second is given by the work that the fields perform on the free electron plasma of the metal. The rate $R_{stim}(N)$ arises from stimulated emission of photons in the gain medium with average carrier number N.

When describing semiconductor (microcavity) lasers, and more recently plasmonic nanolasers[2,25,26] using rate analysis, one finds that a confinement factor Γ must be introduced in the rate equations due to the imperfect spatial overlap of the mode profile with the gain section. This confinement factor expresses the fact that the mode volume V_{eff}, which connects the photon density s to the photon number $S = V_{eff}s$, is distinct from the active (gain) volume V_a, and it is defined as $\Gamma \equiv V_a/V_{eff}$[27].

The confinement factor Γ enters the rate of stimulated emission

$$R_{stim}(N) = \Gamma v_g \zeta g(N) \,, \tag{9}$$

as does a group velocity v_g (at this point the specific type of group velocity is not fixed), a factorization parameter ζ and the bulk gain coefficient $g(N) = g(\Delta N) = \sigma_a \Delta N$. The specific definition of the confinement factor and its physical interpretation then determines which group velocity must be used. We follow Chang and Chuang[27] and choose

$$\Gamma \quad = \quad \frac{\int_{V_a} d^3r\, \frac{1}{2}\varepsilon_0 \left[\partial(\omega\varepsilon'_a)/\partial\omega + \varepsilon'_a\right] |\mathbf{E}|^2}{\int_V d^3r\, U} \approx \frac{2\int_{V_a} d^3r\, U_E}{\int_V d^3r\, U} \,, \tag{10}$$

which identifies v_g as the *material* group velocity of the gain material $v_g = v_{g,a} = c/n_g$ with $n_g = \partial(\omega n'_a)/\partial\omega$. The approximation on the rhs of Eq. (10) is valid for a weakly dispersive gain material with $v_{g,a} \approx v_{ph,a} = c/n'_a$. The factorization parameter ζ measures the degree of inhomogeneity of the inversion profile (spatial hole-burning) and is defined as

$$\zeta = \frac{\int_{V_a} d^3r\, \overline{\Delta N(\mathbf{r},t)} \cdot \overline{\mathbf{E}^2(\mathbf{r},t)}}{\Delta N(t) \cdot \int_{V_a} d^3r\, \overline{\mathbf{E}^2(\mathbf{r},t)}} \,. \tag{11}$$

with the average inversion density $\Delta N(t) = V_a^{-1} \int_{V_a} d^3r\, \overline{\Delta N(\mathbf{r},t)}$. Equation (11) expresses a functional dependence of $\zeta(t)$ on the inversion and field intensity profiles and hence an implicit transient dynamics that stabilises when the laser reaches steady state. In lasers that exhibit negligible spatial hole-burning effects, $\zeta(t)$ is close to unity and can be approximated by a constant factor $\zeta \approx 1$. A time-constant ζ smaller than 1 can also be assumed when the spatial distribution of the inversion and the mode profiles vary only little with time. In these cases, a linear relationship between the stimulated emission rate and the inversion density follows, $R_{stim} \propto \Delta N$, a functional dependence that is commonly adopted in rate equation analyses[2].

For further comparison we calculate the stimulated emission rate R_{stim} from the dynamic change of the total energy, which we are able to extract in FDTD simulations using a rate retrieval method based on Poynting's theorem[14,28]. From Eq. (9) and the knowledge of the confinement factor and average inversion, it is then possible to calculate the factorization parameter ζ. We also compare the confinement factor Γ of the rate equation analysis to the energy confinement

$$\Gamma_E = \int_{V_a} d^3r\, U \Big/ \int_V d^3r\, U, \tag{12}$$

which is defined as the electromagnetic energy in the gain section divided by the total energy of the lasing mode. The two confinement factors will differ in strongly guiding or plasmonic systems because of the modal character of the fields, i.e. an unequal distribution of the electromagnetic energy into electric and magnetic components.

As a side note, recent publications on plasmonic nanolasers have suggested the use of a confinement factor defined to incorporate the average energy (or waveguide group) velocity v_E of the underlying waveguide system of the nanolaser[25,26]. This is possible because the stimulated emission rate R_{stim} and the bulk gain coefficient $g(N)$ in Eq. (9) are invariant to the definition of the effective mode volume, while the confinement factor relates to the group velocity v_g used.

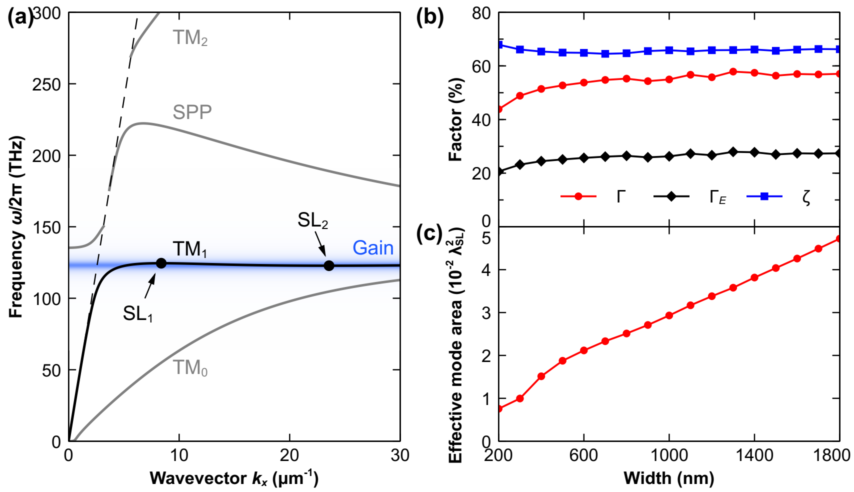

Fig. 7 (a) Complex-frequency dispersion of the plasmonic heterostructure with $h = 110\,\mathrm{nm}$ and $t = 50\,\mathrm{nm}$ (see Fig. 8a). Two SL points in the TM_1 mode with large wavevectors align with the gain spectrum. (b) Lasing properties of the mode for different gain widths. Shown are the confinement factor, the energy confinement and the factorization parameter ζ. (c) The effective mode area $A_{\mathrm{eff}} = A_{\mathrm{g}}/\Gamma$.

The distinction into confinement factor and group velocity can therefore be made in terms of waveguide properties, describing the amplification of a wave packet when it travels along the active waveguide with energy velocity v_E. Comparing Γ' in $R_{\mathrm{stim}}(\Delta N) = v_E\Gamma'\zeta g(N)$[25,26] to Γ in Eq. (10), we find the effective confinement factor $\Gamma' = \Gamma v_{\mathrm{g,a}}/v_E$. The pre-factor $v_{\mathrm{g,a}}/v_E$ points towards effective confinement factors Γ' that can become larger than unity in waveguiding systems with low energy velocity. This also implies a divergence of Γ' as $v_E \to 0$, i.e., in the stopped-light regime. Clearly then, Γ' is not suitable for the description of the stationary lasing mode in the SL laser, in particular considering that the stimulated emission rate into the mode, R_{stim}, does not diverge.

5 Dynamics of stopped-light surface-plasmon polariton lasing

Our analysis of the lasing dynamics shows that the lasing mode localises in-plane to the subwavelength gain region even though there is no cavity that would encourage this behaviour. Moreover, possible gain-guiding effects would in typical semiconductor gain materials even promote an anti-guiding rather than a guiding. To explain the mechanism that governs the formation of the subwavelength modes we now analyse a structure that supports stopped-light lasing/spasing at higher wave numbers k, i.e. consider coherent amplification of stopped surface-plasmon polaritons (a new form of spasing) using a plasmonic-mode design of the metal-dielectric stack structure that allows for a stopped-"light" singularity in the density of state and surface-plasmon polariton amplification.

In contrast to conventional single-mode lasing where the lasing frequency and mode profile are determined by the cavity, the SL lasing mode is characterised by

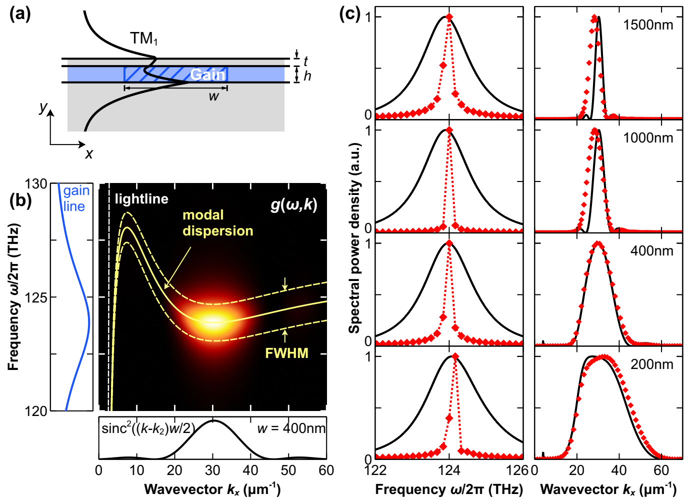

Fig. 8 (a) E_x field profile of the TM_1 waveguide mode in the plasmonic heterostructure waveguide. (b) Detail of the TM_1 mode's complex frequency dispersion (yellow line) exhibiting two SL points with zero slope. The dispersion is overlaid over the semi-analytical results for the coupling strength $g(\omega, k)$. The gain spectrum in blue and the spatial sinc^2-function centred at the second SL point are given to the left and below the main graph. (c) Predicted lasing frequency on the left and wavevector spectrum on the right. Simulation results in red are compared to the semi-analytical result of $G(\omega) = \int \mathrm{d}k\, g(\omega, k)$ in black.

a closed-loop energy vortex and forms dynamically by phase-locking the continuum of k-modes in the vicinity of the SL points. During the transient phase the lasing/spasing mode acquires a spectral composition that maximises the effective gain

$$G(\omega) \propto \int \mathrm{d}k\, \mathcal{L}(\omega - \omega_0) \cdot D(\omega, k) \cdot \mathrm{sinc}^2\left(\left(k - k'\right) w/2\right) = \int \mathrm{d}k\, g(\omega, k), \quad (13)$$

where k' is centred on one of the SL singularities, by balancing the spatial confinement of the lasing mode to the gain section against its spectral overlap with

Symbol	Description	Value
$\omega_e/2\pi$ (λ_e)	Emission frequency (wavelength)	123.89 THz (2419.7 nm)
γ_e	Emission spectral half-width	$1/(63.085\,\mathrm{fs}) \approx 15.85\,\mathrm{ps}^{-1}$ ($\sim$49 nm)
$\sigma_{0,e}$	Emission cross-section	$2.12 \cdot 10^{-15}\,\mathrm{cm}^2$
N	Carrier density	$2 \cdot 10^{18}\,\mathrm{cm}^{-3}$
g_e	Maximum gain coefficient	$4240\,\mathrm{cm}^{-1}$

Table 2 Gain medium parameters for emission into the second stopped light point of the bound TM_1 waveguide mode.

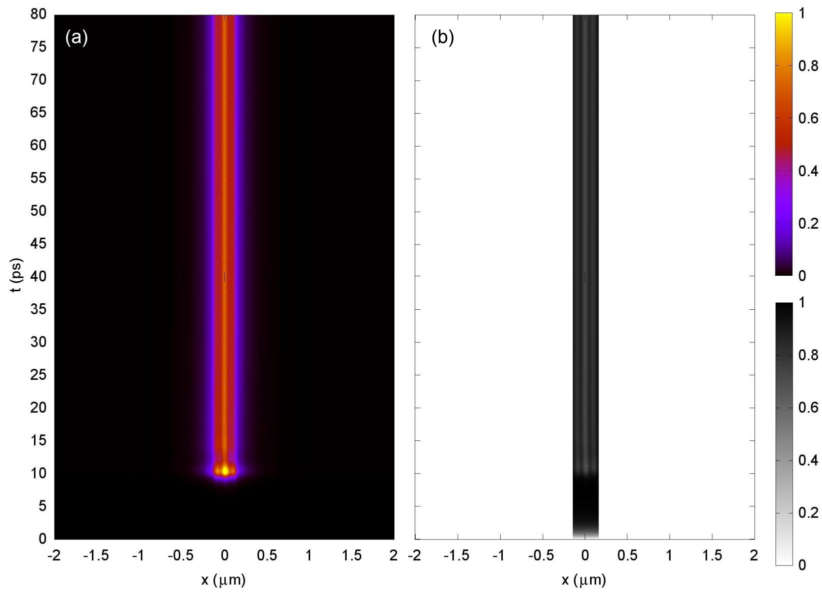

Fig. 9 Spatio-temporal dynamics of the stopped-light surface-plasmon polariton laser for a gain section width of 300 nm. Shown are the cycle-averaged electromagnetic energy density (a) and the inversion in the gain material (b). The cut along the x-axis is taken 30 nm above the metal substrate inside the waveguide core.

the gain line $\mathcal{L}(\omega - \omega_0)$. The density of states

$$D(\omega, k) \propto \frac{\gamma(k)}{(\omega(k) - \omega)^2 + \gamma^2(k)} \tag{14}$$

of the (TM_2) waveguide mode plays a critical role in this process as it links and controls the spatial and spectral overlap. The close agreement of the analytically predicted frequencies ω_{SLL} and k-spectra, $g(\omega_{\mathrm{SLL}}, k)$, with those retrieved from full spatio-temporal simulations (Fig. 8c) confirms this principle: the frequency ω_{SLL} of the SL lasing mode is selected by maximization of $G(\omega)$, and its mode shape is determined by $g(\omega_{\mathrm{SLL}}, k)$. While the results further suggest that there is no fundamental limit for the spatial compression of the mode, a higher localization would of course require an increasingly flat dispersion to maintain a high spectral overlap.

With bound plasmonic modes one can exploit a wide range of wavevectors and achieve considerably smaller effective mode volumes than for photonic modes. We optimised the waveguide dispersion (Fig. 7 and Fig. 8) to exhibit two stopped light points in the plasmonic TM_1 mode at $\omega_1/2\pi = 128.14\,\mathrm{THz}$ ($\lambda_1 \approx 2339.6\,\mathrm{nm}$) at $k_1 = 7.41\,\mu\mathrm{m}^{-1}$ and $\omega_2/2\pi = 123.89\,\mathrm{THz}$ ($\lambda_2 \approx 2419.7\,\mathrm{nm}$) at $k_2 = 30.34\,\mu\mathrm{m}^{-1}$. There is no out-coupling to propagating free-space waves and the modal loss is approximately 3 times larger than the total loss of the TM_2 waveguide mode due to the higher field localization. Figure 8b shows the predicted coupling strength $g(\omega, k)$ for a plasmonic stopped-light lasing structure. We choose to tune the emission line of the gain medium to the frequency of the

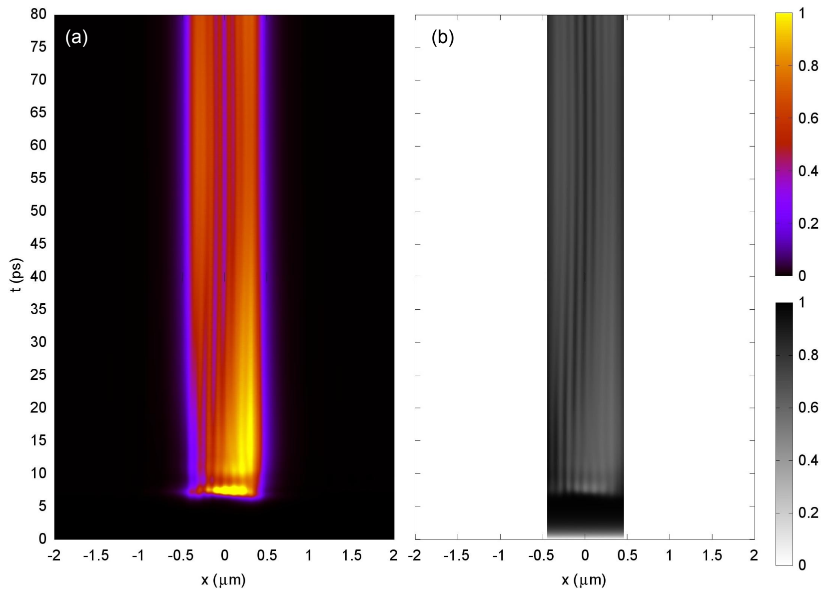

Fig. 10 Spatio-temporal dynamics of the stopped-light surface-plasmon polariton laser for a gain section width of 900 nm. Shown are the cycle-averaged electromagnetic energy density (a) and the inversion in the gain material (b). The cut along the x-axis is taken 30 nm above the metal substrate inside the waveguide core.

second SL point ω_2 (Table 2) and consequently shift the peak of the the sinc^2-function to k_2. The broad spectrum of supported wavevectors allows for localization of the SL lasing mode down to gain sections with a width of $w = 200$ nm (Fig. 7). For these small gain sections the maximum of the field profile aligns over the gain, effectively locking the amplitude and phase of the complementary modes with positive and negative phase velocities in space.

Figure 9 demonstrates that the locking of the complementary modes in space takes place from the onset of the relaxation oscillations and remains constant in time for small gain section widths. The figure shows the spatio-temporal dynamics of the cycle-averaged energy density (left) and gain material inversion (right) inside the waveguide core 30 nm above the metal substrate for a width of the $w = 300$ nm. After the initial build-up of inversion, a single relaxation oscillation leads into a steady-state regime with a spatially constant energy density profile. The profile is symmetric with respect to the centre of the gain section and is mirrored by the inversion where regions of smaller inversion are linked to corresponding regions of high field intensity due to depletion. As the spectrum of wavevectors is centred at a non-zero wavevector k_2 (see Fig. 8) the lasing mode becomes spatially modulated along x with nodes every $\pi/k_2 \approx 100$ nm.

For wider gain sections the positions of the nodal planes can move in time depending on the contributions to the lasing mode from the counterpropagating waveguide modes. Figure 10 shows an exemplary time series for the case of a gain section of 900 nm width. Relaxation oscillations start earlier than for the smaller gain section and their spatial profile is no longer symmetric with respect

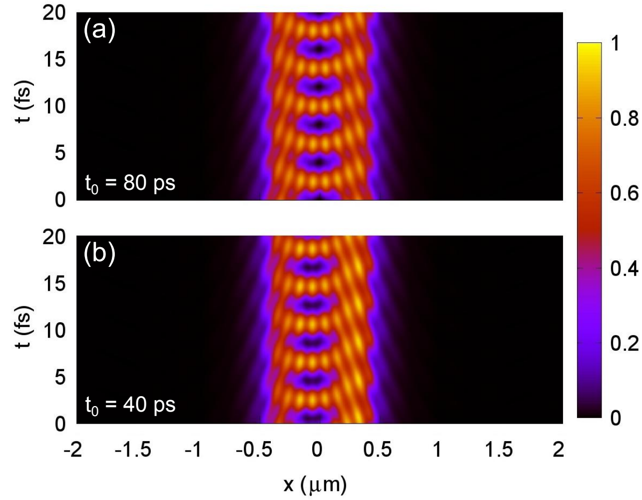

Fig. 11 Ultrafast spatio-temporal dynamics (non cycle-averaged) of the (surface-plasmon polariton) energy density on the femtosecond timescale. The window of 20 femtosecond reveals the underlying ultrafast dynamics as shown in Fig. 10 after 80 ps (a) and 40 ps (b). The standing wave pattern in the centre is easily distinguishable from the propagating waves at the sides. The colour has been rescaled to the maximum energy density value and is not the same as in Fig. 10.

to the centre of the section. Initially, the left-propagating waveguide mode has a higher amplitude leading to a high energy density with little spatial variation on the right and a standing wave pattern with lower amplitude on the left of the gain section. Again, this is mirrored in the (gain material) inversion shown in Fig. 10(b).

The superposition of propagating and standing wave SPPs reveals itself in the spatio-temporal dynamics on the femtosecond timescale as shown in Fig. 11; the upper frame (Fig. 11(a)) illustrates the spatio-temporal dynamics of Figure 10 in a time-interval of 20 femtoseconds starting at $t_0 = 80\,\mathrm{ps}$ and the lower frame shows the corresponding frame starting at $t_0 = 40\,\mathrm{ps}$. In both cases, the phase fronts are seen to move inwards. But as time progresses from the earlier frame (Fig. 11(b)), the right-propagating waveguide mode becomes stronger, resulting in a more pronounced standing wave pattern that slowly moves towards the centre of the gain section. This behaviour is a direct consequence of the cavity-free property of SL lasing, where forward and backward modes become uncoupled due to the absence of back-reflections at geometric boundaries and form independently. At the end of the 80 picosecond time interval shown in Figure 10, Fig. 11(a) shows that the profiles have become symmetric, just as was observed for small gain sections.

The richest ultrafast spatio-temporal dynamics, however, emerges in wide gain sections as epitomised in Fig. 12 for $w = 2000\,\mathrm{nm}$. Relaxation oscillations start independently at the edges of the gain section and several, clearly visible oscillations take place. During the relaxation oscillations a standing wave SPP component is formed close to the centre of the gain section which seems to per-

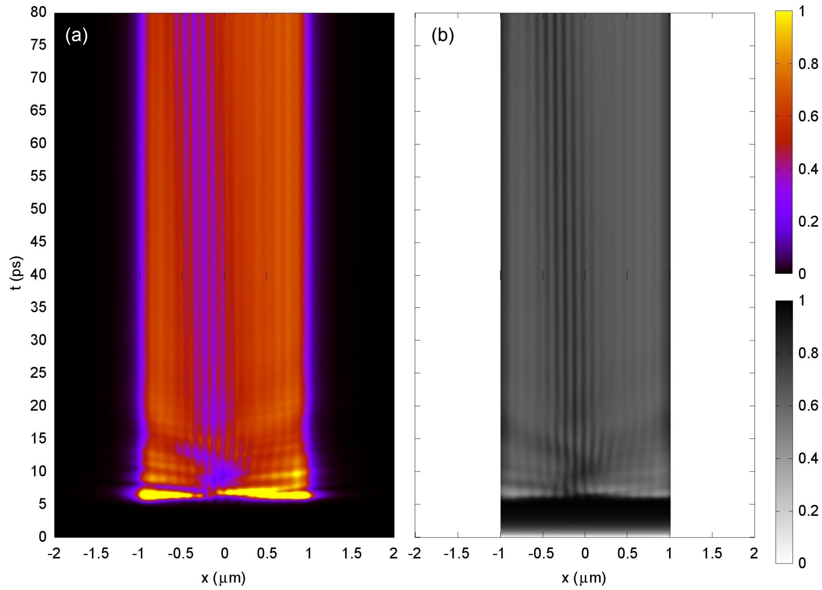

Fig. 12 Spatio-temporal dynamics of the stopped-light surface-plasmon polariton laser for a gain section width of 2000 nm. Shown are the cycle-averaged electromagnetic energy density (a) and the inversion in the gain material (b). The cut along the *x*-axis is taken 30 nm above the metal substrate inside the waveguide core.

form an oscillatory motion in space. After approximately 20 ps, a quasi-steady state profile is reached, that now evolves on a much slower timescale than during the dynamics during the initial relaxation oscillations. In contrast to the cases of Figure 9 and Figure 10 , the system now does not evolve into a more symmetric state within the timescales shown here. Instead, the standing wave pattern is seen to drift away from the centre towards the edge of the gain section. Judging the complexity of the spatio-temporal behaviour it is not clear at all if the dynamics will eventually lead to a symmetric steady state for very long times, as once an asymmetry is present in a nonlinear system it tends to prevail as a spatio-temporally varying structure.

6 Conclusions and outlook

Nanoplasmonic stopped-light lasing is a recently established principle [18] that may not only open the door to ultrafast cavity-free nanolasing, ultra-thin lasing surfaces and cavity-free quantum-electrodynamics but also provide an entry point to quantum gain in quantum plasmonics [29] and quantum fluids of light [30]. Here, following these principles, we have studied its spatio-temporal dynamics, and, particularly, the ultrafast femto- and picosecond dynamics of surface plasmon polariton cavity-free nanolasing enabled by dispersion-less stopped-“light”.

Engineered singularities in the density of optical states realised in a metal-dielectric-metal nano-waveguide structure are confirmed to lead to a stopped-light feedback mechanism that is the basis for the dynamic observed cavity-free photonic and surface-plasmon polariton nanolasing.

Having established a theoretical framework for characteristic laser parameters (such as the confinement factor) and deriving effective laser rate equations for cavity-free stopped-light nanolasing allowed us to explain the link with and expose the differences to traditional laser rate equations describing conventional lasers.

Extensive simulations on the basis of a full-time domain Maxwell-Bloch Langevin approach in combination with (semi-) analytic theory have uncovered that in the absence of cavity-induced feedback a phase-locked superposition of quasi dispersion-free waveguide mode promotes the dynamic formation of a subwavelength lasing mode. Our simulations have further demonstrated that this mechanism proves to be remarkably robust against interface roughness and observed spontaneous emission factor $\beta \approx 0.9$ is a manifestation of a very high coupling of spontaneous emission into the stopped-light mode.

The ultrafast femto- and picosecond dynamics of stopped-light surface plasmon polariton lasing is shown to be stable for gain sections of a width of up to around 200 nm. In wider gain structures of the order of 1 μm, the initial dynamics is characterised by spatio-temporally oscillating amplified surface-plasmon polaritons on ultrafast timescales <5 femtoseconds and with spatial periods on the nanoscale <100 nm. Remarkably, this formation of a complex spatio-temporal SPP pattern has a surprising outward resemblance with the characteristic spatio-temporal light-field dynamics found in broad-area semiconductor lasers about 20 years ago[31–33]. But now the dynamics is much faster, happens on much smaller scales and is coherent.

Acknowledgements

This research was supported by the Leverhulme Trust and the Engineering and Physical Sciences Research Council (EPSRC) UK.

References

1 M. T. Hill, Y.-S. Oei, B. Smalbrugge, Y. Zhu, T. de Vries, P. J. van Veldhoven, F. W. M. van Otten, T. J. Eijkemans, J. P. Turkiewicz, H. de Waardt, E. J. Geluk, S.-H. Kwon, Y.-H. Lee, R. Ntzel and M. K. Smit, *Nat. Photon.*, 2007, **1**, 589–594.
2 R. F. Oulton, V. J. Sorger, T. Zentgraf, R.-M. Ma, C. Gladden, L. Dai, G. Bartal and X. Zhang, *Nature*, 2009, **461**, 629–632.
3 M. A. Noginov, G. Zhu, A. M. Belgrave, R. Bakker, V. M. Shalaev, E. E. Narimanov, S. Stout, E. Herz, T. Suteewong and U. Wiesner, *Nature*, 2009, **460**, 1110–1112.
4 R.-M. Ma, R. F. Oulton, V. J. Sorger, G. Bartal and X. Zhang, *Nat. Mater.*, 2011, **10**, 110–113.
5 M. Khajavikhan, A. Simic, M. Katz, J. H. Lee, B. Slutsky, A. Mizrahi, V. Lomakin and Y. Fainman, *Nature*, 2012, **482**, 204–207.
6 Y.-J. Lu, J. Kim, H.-Y. Chen, C. Wu, N. Dabidian, C. E. Sanders, C.-Y. Wang, M.-Y. Lu, B.-H. Li, X. Qiu, W.-H. Chang, L.-J. Chen, G. Shvets, C.-K. Shih and S. Gwo, *Science*, 2012, **337**, 450–453.
7 K. J. Vahala, *Nature*, 2003, **424**, 839–846.
8 S. L. McCall, A. F. J. Levi, R. E. Slusher, S. J. Pearton and R. A. Logan, *Appl. Phys. Lett.*, 1992, **60**, 289–291.
9 K. Iga, F. Koyama and S. Kinoshita, *IEEE J. Quantum Electron.*, 1988, **24**, 1845–1855.
10 O. Painter, R. K. Lee, A. Scherer, A. Yariv, J. D. O'Brien, P. D. Dapkus and I. Kim, *Science*, 1999, **284**, 1819–1821.

11 H. Altug, D. Englund and J. Vuckovic, *Nat. Phys.*, 2006, **2**, 484–488.
12 D. J. Bergman and M. I. Stockman, *Phys. Rev. Lett.*, 2003, **90**, 027402.
13 P. Berini and I. De Leon, *Nat. Photon.*, 2011, **6**, 16–24.
14 O. Hess, J. B. Pendry, S. A. Maier, R. F. Oulton, J. M. Hamm and K. L. Tsakmakidis, *Nat. Mater.*, 2012, **11**, 573–584.
15 J. B. Khurgin and G. Sun, *Nat. Photon.*, 2014, **18**, 10–14.
16 H. Cao, *Wave Random Media*, 2003, **13**, R1–R39.
17 D. S. Wiersma, *Nat. Phys.*, 2008, **4**, 359–367.
18 T. Pickering, J. M. Hamm, A. F. Page, S. Wuestner and O. Hess, *Nat. Comm.*, 2014, **5**, 4972.
19 A. Pusch, S. Wuestner, J. M. Hamm, K. L. Tsakmakidis and O. Hess, *ACS Nano*, 2012, **6**, 2420–2431.
20 T. Baba, *Nat. Photon.*, 2008, **2**, 465–473.
21 S. Mookherjea, J. S. Park, S.-H. Yang and P. R. Bandaru, *Nat. Phot.*, 2008, **2**, 90–93.
22 K. L. Tsakmakidis, T. W. Pickering, J. M. Hamm, A. F. Page and O. Hess, *Phys. Rev. Lett.*, 2014, **112**, 167401.
23 R.-M. Ma, R. F. Oulton, V. J. Sorger and X. Zhang, *Laser Photon. Rev.*, 2012, **7**, 1–21.
24 G. Björk and Y. Yamamoto, *IEEE J. Quant. Electron.*, 1991, **27**, 2386–2396.
25 C. Z. Ning, *Phys. Status Solidi B*, 2010, **247**, 774–788.
26 K. Ding and C. Z. Ning, *Light: Science & Applications*, 2012, **1**, e20.
27 S.-W. Chang and S. L. Chuang, *IEEE J. Quant. Electron.*, 2009, **45**, 1014–1023.
28 J. M. Hamm, S. Wuestner, K. L. Tsakmakidis and O. Hess, *Phys. Rev. Lett*, 2011, **107**, 167405.
29 M. S. Tame, K. R. McEnery, . K. Özdemir, J. Lee, S. A. Maier and M. S. Kim, *Nat. Physics*, 2013, **9**, 329–340.
30 I. Carusotto and C. Ciuti, *Rev. Mod. Phys.*, 2013, **85**, 299–366.
31 O. Hess and T. Kuhn, *Phys. Rev. A*, 1996, **54**, 3347–3359.
32 O. Hess and T. Kuhn, *Phys. Rev. A*, 1996, **54**, 3360–3368.
33 E. Gehrig and O. Hess, *Spatio-Temporal Dynamics and Quantum Fluctuations in Semiconductor Lasers*, Springer, 2003.

